Monthly Notices
of the
ROYAL ASTRONOMICAL SOCIETY

MNRAS **491,** 1093–1103 (2020)
Advance Access publication 2019 August 19

doi:10.1093/mnras/stz2286

Ionizing the intergalactic medium by star clusters: the first empirical evidence

E. Vanzella,[1]★† G. B. Caminha,[2] F. Calura,[1] G. Cupani,[3] M. Meneghetti,[1] M. Castellano,[4] P. Rosati,[1,5] A. Mercurio,[6] E. Sani,[7] C. Grillo,[8] R. Gilli,[1] M. Mignoli,[1] A. Comastri,[1] M. Nonino,[3] S. Cristiani,[3] M. Giavalisco[9] and K. Caputi[2]

[1]*INAF – OAS, Osservatorio di Astrofisica e Scienza dello Spazio di Bologna, via Gobetti 93/3, I-40129 Bologna, Italy*
[2]*Kapteyn Astronomical Institute, University of Groningen, Postbus 800, NL-9700 AV Groningen, the Netherlands*
[3]*INAF – Osservatorio Astronomico di Trieste, via G. B. Tiepolo 11, I-34143 Trieste, Italy*
[4]*INAF – Osservatorio Astronomico di Roma, Via Frascati 33, I-00078 Monte Porzio Catone (RM), Italy*
[5]*Dipartimento di Fisica e Scienze della Terra, Università degli Studi di Ferrara, via Saragat 1, I-44122 Ferrara, Italy*
[6]*INAF – Osservatorio Astronomico di Capodimonte, Via Moiariello 16, I-80131 Napoli, Italy*
[7]*European Southern Observatory, Alonso de Cordova 3107, Casilla 19, Santiago 19001, Chile*
[8]*Dipartimento di Fisica, Università degli Studi di Milano, via Celoria 16, I-20133 Milano, Italy*
[9]*Astronomy Department, University of Massachusetts, Amherst, MA 01003, USA*

Accepted 2019 August 14. Received 2019 July 26; in original form 2019 April 16

ABSTRACT

We present a VLT/X-Shooter spectroscopy of the Lyman continuum (LyC) emitting galaxy *Ion2* at $z = 3.2121$ and compare it to that of the recently discovered strongly lensed LyC emitter at $z = 2.37$, known as the *Sunburst* arc. Three main results emerge from the X-Shooter spectrum: (a) the Ly α has three distinct peaks with the central one at the systemic redshift, indicating a ionized tunnel through which both Ly α and LyC radiation escape; (b) the large O32 oxygen index ([O III] $\lambda\lambda$4959, 5007/[O II] $\lambda\lambda$3727, 3729) of $9.18^{+1.82}_{-1.32}$ is compatible to those measured in local ($z \sim 0.4$) LyC leakers; (c) there are narrow nebular high-ionization metal lines with $\sigma_v < 20$ km s^{-1}, which confirms the presence of young hot, massive stars. The He II λ1640 appears broad, consistent with a young stellar component including Wolf–Rayet stars. Similarly, the *Sunburst* LyC emitter shows a triple-peaked Ly α profile and from VLT/MUSE spectroscopy the presence of spectral features arising from young hot and massive stars. The strong lensing magnification, ($\mu > 20$), suggests that this exceptional object is a gravitationally bound star cluster observed at a cosmological distance, with a stellar mass $M \lesssim 10^7$ M$_\odot$ and an effective radius smaller than 20 pc. Intriguingly, sources like Sunburst but without lensing magnification might appear as *Ion2*-like galaxies, in which unresolved massive star clusters dominate the ultraviolet emission. This work supports the idea that dense young star clusters can contribute to the ionization of the IGM through holes created by stellar feedback.

Key words: gravitational lensing: strong – galaxies: formation – galaxies: starburst.

1 INTRODUCTION

Recently, extensive surveys attempting to identify and study galaxies emitting Lyman continuum (LyC) radiation across a large range of cosmic time have yielded several low-redshift cases whose properties are believed to be representative of the galaxies at redshift $z > 7$ that contributed the radiation that has reionized the Universe. Since the direct detection of ionizing radiation from the epoch of reionization (EoR) is not possible because of the cosmic opacity, the low-redshift 'analogues' of the distant galaxies play a key role in understanding the mechanisms that allow the escape of ionizing radiation from star-forming galaxies (e.g. Dayal & Ferrara 2018).

The census of LyC galaxies is growing fast, both in the nearby Universe (Izotov et al. 2018, and references therein) and at high redshift, i.e. $z \approx 3.5$ (de Barros et al. 2016; Shapley et al. 2016; Vanzella et al. 2016b, 2018; Bian et al. 2017), and relevant progress has recently been made in a statistical sense by analysing dozens of

★ E-mail: eros.vanzella@inaf.it
† Based on observations collected at the European Southern Observatory under ESO programmes P0102.A-0391(A) and DDT-297.A-5012(A).

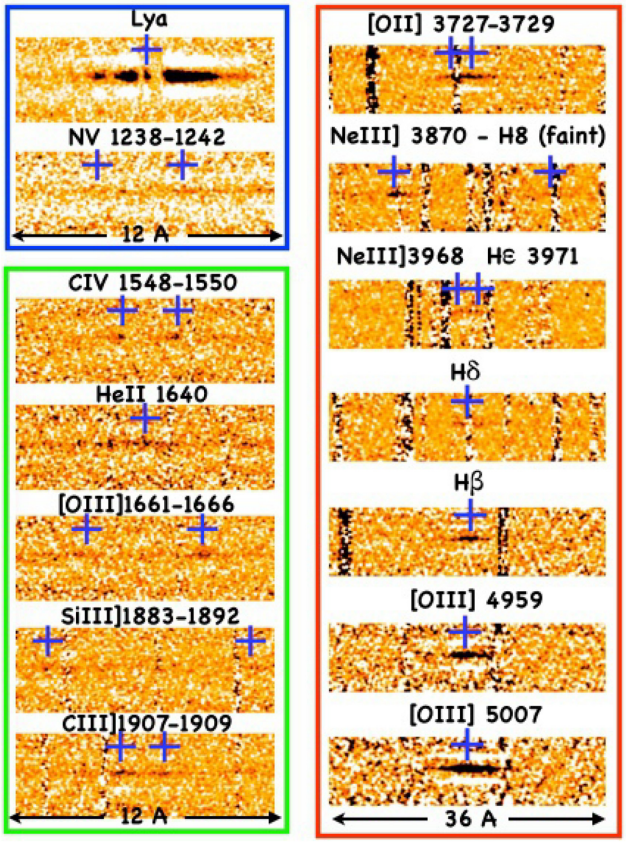

Figure 1. The most relevant atomic transitions of *Ion2* in the VLT/X-Shooter UVB ($R = 5300$), VIS ($R = 8900$), and NIR ($R = 5600$) arms, colour coded in blue, green, and red boxes, respectively. The expected positions at a systemic redshift $z = 3.2121$ are indicated with blue symbols ('+'). For each transition, the corresponding rest-frame wavelength is reported. The rest-frame wavelength width of the zoomed spectra is reported at the bottom, for each arm. The significance of the reported transitions is summarized in Table 1.

high-redshift galaxies with dedicated *HST* imaging (e.g. Japelj et al. 2017; Fletcher et al. 2019) and deep spectroscopy (e.g. Marchi et al. 2018; Steidel et al. 2018). In particular, a positive correlation among LyC escape and Ly α equivalent width has been inferred, as well as an apparently higher *fesc* at fainter ultraviolet magnitudes, such that galaxies might account to more than 50 per cent of the ionizing budget at $z \sim 3$ (Steidel et al. 2018). Spectral features like the profile of the escaping Ly α line, the strength of the low-ionization interstellar absorption lines tracing the covering fractions of neutral gas (e.g. [C II] λ1334, [Si II] λ1260), and the line ratios tracing the ionization- or density-bounded conditions in the interstellar medium (like the O32 index, [O III] $\lambda\lambda$4959, 5007/[O II] $\lambda\lambda$3727, 3729) hold the promise to provide useful diagnostics of the mechanisms that govern the escape of ionizing radiation, although we currently do not yet know which properties provide necessary and/or sufficient conditions for this to happen (e.g. Jaskot & Oey 2013; Reddy et al. 2016, 2018; Schaerer et al. 2016; Grazian et al. 2017; Verhamme et al. 2017; Chisholm et al. 2018; Gazagnes et al. 2018; Izotov et al. 2018; Steidel et al. 2018; McKinney et al. 2019). While the current growing samples serve as a reference for the identification of cosmic reionizers, the physical processes that made these galaxies transparent to LyC radiation are yet to be understood. The way ionized channels are carved in the interstellar medium is under continuous investigation, especially in the local Universe (Herenz et al. 2017; Micheva et al. 2017, 2019; Bik et al. 2018; Kehrig et al. 2018) where the detection of LyC radiation is instrumental to catch such episodes in the act (e.g. Heckman et al. 2011). It remains unclear what is the spatial distribution of the escaping ionizing radiation, the porosity and the kinematics of the neutral gas, and the role the internal constituents of high-z LyC galaxies (namely, the star-forming complexes, OB-associations, young massive clusters, and massive stars) have in carving such ionized regions. In general, the small physical scales, likely of the order of a few tens of pc and in which such constituents originate, are still unreachable at cosmological distances (e.g. a typical *HST* pixel of 30 milliarcsec subtends 250–300 pc at $z \sim 2$–6, encompassing one or more star-forming complexes). This limitation is even worse when ground-based seeing-limited spectroscopy is performed.

This work presents new VLT/X-Shooter spectroscopy of a LyC galaxy dubbed *Ion2* (Vanzella et al. 2016b), and VLT/MUSE observation of the recently discovered strongly lensed LyC emitter at $z = 2.37$ (known as Sunburst arc; Dahle et al. 2016; Rivera-Thorsen et al. 2017, 2019). The similarity between the exceptional strongly lensed Sunburst and *Ion2* sheds light on the possible 'engine' behind the spatially unresolved high-z LyC leakers, like *Ion2*. We make use of archival VLT/MUSE and *HST*/ACS data targeting the Sunburst object with the aim to emphasize and explore this connection.

We assume a flat cosmology with $\Omega_M = 0.3$, $\Omega_\Lambda = 0.7$, and $H_0 = 70$ km s^{-1} Mpc^{-1}.

2 THE LYMAN CONTINUUM GALAXY *ION2*

Ion2 is a well-known LyC emitter at $z = 3.2121$ lying in the CDFS showing an escape fraction higher than 50 per cent (Vanzella et al. 2015, 2016b). Here we present new VLT/X-Shooter observations that improve (in terms of depth, spectral resolution, and wavelength coverage) our previous analysis (de Barros et al. 2016).

2.1 X-Shooter observations

Ion2 was observed during 2018 November for a total integration time of 5 h under optimal seeing conditions, typically 0.5–0.7 arcsec. The slit widths were 1.0, 0.9, and 0.9 arcsec, corresponding to a spectral resolution of $R = 5400$, 8900, and 5600 in the UVB, VIS, and NIR arms, respectively [Prog. 0102.A-0391(A), P.I. Vanzella]. Given the good seeing, the aforementioned resolution values must be considered as lower limits. The data reduction was carried on as described in several previous works (we refer the reader to Vanzella et al. 2016a, 2017b), in which the AB-BA sky subtraction scheme was implemented with single exposures of 915, 946, and 900 s on each of the three UVB, VIS, and NIR arms, respectively. The target was dithered 2.4 arcsec along the slit. The spectral range from the U to K bands covers the rest-frame wavelengths, which include the Ly α and the optical lines [O III] $\lambda\lambda$4959, 5007. The continuum is barely detected, from which a dozen of emission lines emerge with S/N ratio spanning the interval 2–50 (see Fig. 1 and Table 1). A careful analysis of the statistical significance of the spectral features is reported in Appendix B1.

2.2 Results

The X-Shooter spectrum shows at least three features not observed with previous spectroscopy (de Barros et al. 2016): a multipeaked Ly α profile, the presence of narrow ultraviolet high-ionization lines,

Table 1. The most relevant atomic transitions of *Ion2* are reported, showing the corresponding zoomed regions on the two-dimensional spectrum of Fig. 1. The S/N ratios indicate the reliability of the lines (see also Appendix B1). 1σ upper limits on the line fluxes are reported in the case of non-detections. The [Ne V] λ3426, H γ, and the [O III] λ4364 are not reported as they lie on the atmospheric absorption bands. Line fluxes are reported in units of 10^{-17} erg s^{-1} cm^{-2} (no slit losses are considered) and the FWHM is expressed in km s^{-1}; the rest-frame equivalent width (EW) is reported in Å and calculated starting from the line fluxes and continuum derived from CANDELS photometry, adopting magnitudes ≃24.45 and ≃24.1 in the optical and near-infrared arms, respectively. The comment 'Narrow' means that the line is not resolved, while 'Broad' stands for resolved but a precise measurement is not feasible.

Line/λ_{vacuum}	Flux($\frac{S}{N}$)(FWHM)(EW)	Redshift (1σ)
Ly α(−2) 1215.7	1.68(8.0)(∼141)(5.7)	3.2044(3)
Ly α(−1) 1215.7	5.28(29.0)(146)(18.0)	3.2096(1)
Ly α(0) 1215.7	0.96(10.5)(<56)(3.3)	3.2121(2)
Ly α(1) 1215.7	20.25(110)(298)(69.1)	3.2164(1)
Ly α(total)	28.16(−)(−)(97.6)	–
N V λ1238.82	<0.12(1.0)(−)(< 0.5)	(3.2121)fixed
N V λ1242.80	<0.12(1.0)(−)(< 0.5)	(3.2121)fixed
C IV λ1548.20	0.28(5.2)(Narrow)(1.5)	(3.2121)fixed
C IV λ1550.78	0.20(4.8)(Narrow)(1.1)	(3.2121)fixed
[He II] λ1640.42	0.45(5.0)(Broad)(2.8)	(3.2121)fixed
[O III] λ1660.81	0.40(3.5)(Narrow)(2.5)	(3.2121)fixed
[O III] λ1666.15	0.65(5.4)(Narrow)(4.2)	(3.2121)fixed
[Si III] λ1882.65	0.30(2.0)(Narrow)(2.4)	(3.2121)fixed
[Si III] λ1892.03	0.15(1.5)(Narrow)(1.2)	(3.2121)fixed
C III] λ1906.68	0.44(6.7)(Narrow)(4.1)	3.2127(5)
C III] λ1908.73	0.35(4.9)(Narrow)(3.2)	(3.2121)fixed
[O II] λ3727–3729	3.5(6.0)(−)(81)	3.2122(3)
Ne III] λ3869.81	1.8(4.0)(−)(45)	3.2119(4)
Ne III] λ3968.53	1.2(1.5)(−)(32)	(3.2121)fixed
H δ λ4102.92	1.1(2.0)(−)(31)	(3.2121)fixed
H β λ4862.69	2.9(6.0)(<60)(114)	3.2120(3)
[O III] λ4960.30	7.4(22.0)(−)(304)	3.2121(2)
[O III] λ5008.24	24.8(65.0)(146)(1040)	3.2121(1)

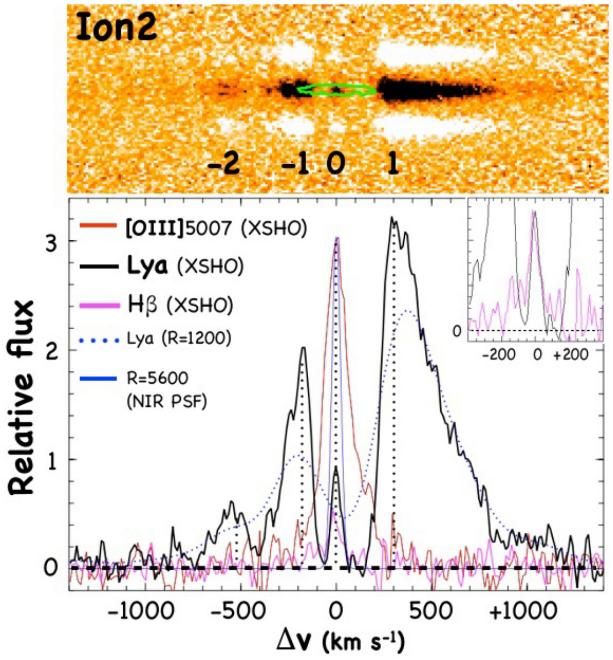

Figure 2. The top panel shows the two-dimensional Ly α of *Ion2* (at a resolution $R = 5300$) with indicated the wavelength position of the [O III] λ5007 (5σ green contour) and the four peaks, labelled as '−2', '−1', '0', and '1'. The peak '0' falls exactly at the [O III] λ5007 redshift. In the bottom panel, the Ly α, [O III] λ5007 (rescaled for clarity) and H β line profiles are superposed in the velocity domain. The inset shows the zoomed region around the zero velocity ($-400 < \Delta v < +400$ km s^{-1}) where the Ly α peak '0' has here been rescaled to match the peak of the H β line with the aim to emphasize the consistency among the widths of the lines. The effect of low spectral resolution is also shown ($R = 1200$, blue dotted line). The Gaussian shape representing the spectral resolution in the NIR arm ($R = 5600$) is also shown for comparison with a solid blue line.

and the new detection of [O II] λλ3727, 3729 and H β optical rest-frame lines. Below we summarize these new results.

(i) The Ly α profile shows three peaks with the central one placed exactly at the systemic redshift ($z = 3.2121$, see Fig. 2), resembling the same Ly α structure observed in another LyC galaxy discovered at $z = 4.0$ (dubbed *Ion3*; Vanzella et al. 2018). This is the fourth confirmed LyC emitter showing a Ly α peak emerging at the systemic velocity. The four objects are also characterized by a quite large escape fraction of ionizing radiation, *fesc* > 50 per cent (Izotov et al. 2018; Vanzella et al. 2018; Rivera-Thorsen et al. 2019). Fig. 3 shows a comparison of the Ly α shapes, and includes *Ion2*, *Ion3*, a high-surface density LyC emitter at $z = 0.4317$ with a very large escape fraction (*fesc* >72 per cent) from the Izotov et al. (2018) sample and Sunburst. In the LyC emitters shown in Fig. 3, the positions of the peaks at the two sides of the central one are different, reflecting different kinematical features characterizing each system. The same line shape has been investigated by Rivera-Thorsen et al. (2017) performing radiative transfer (RT) calculations in the framework of three different scenarios including the expanding shell models (Schaerer et al. 2011; Gronke, Bull & Dijkstra 2015): a density-bounded medium, picket-fence medium, and the presence of a ionized channel embedded in the H I shell. Only the last case suitably reproduces the triple-peaked Ly α profile: a significant amount of H I gas with a perforated channel accounts for both the typical Ly α broadening by frequency diffusion (peaks far from the resonance frequency, e.g. '−2, −1, + 1') and the superimposed Ly α emission at zero velocity (peak '0'). Additionally, as discussed by Rivera-Thorsen et al. (2017), the profile of the non-scattered Ly α photons escaping through an optically thin tunnel would resemble the width of the Balmer emission lines, which would represent a proxy of the intrinsic Ly α shape before undergoing any RT effect. The brightest Balmer emission we have in the spectrum is the H β line detected with an S/N = 6. Fig. 2 superimposes the central Ly α peak ('0') and the H β, which show compatible widths (being both marginally resolved; see Table 1). This is fully in line with what was predicted by Behrens, Dijkstra & Niemeyer (2014) (see their fig. 7). It is also worth stressing that the detection of the above narrow Ly α features has been possible only thanks to the high spectral resolution ($R > 5000$) achievable with X-Shooter (see the case $R = 1200$ in Fig. 2), underlying the fact that the Ly α line can be a powerful probe of optically thin media up to $z = 4$ (and possibly up to $z = 6.5$ in the case of transparent IGM, e.g. Matthee et al. 2018).

(ii) The C IV λλ1548, 1550, O III] λλ1661, 1666, He II λ1640, and the C III] λλ1907, 1909 high-ionization emission lines have been detected (see Fig. 1 and Table 1), with the doublets being well separated. It is worth noting that all the nebular metal lines appear very narrow and possibly not resolved ($\sigma_v < 20$ km s^{-1}), while the He II λ1640 emission, despite a relatively low S/N, is clearly broader. To emphasize such a difference, Fig. 4 shows the portion of the X-Shooter two-dimensional spectrum containing the

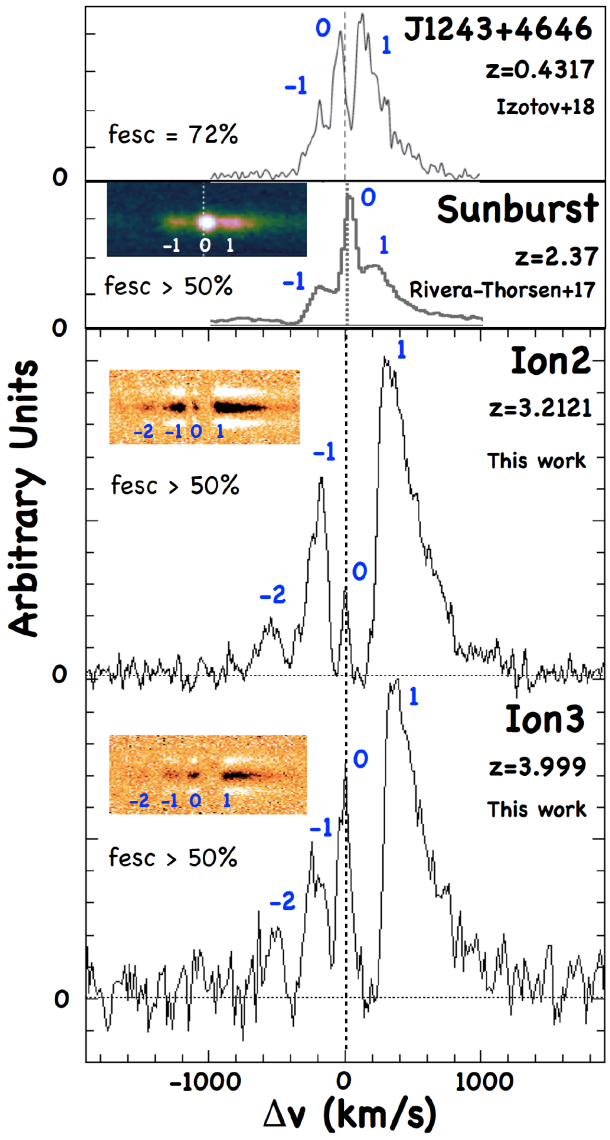

Figure 3. Ly α profiles in the velocity space of all the LyC emitters with triple-peaked Ly α emission currently known. The upper two panels have been adapted from Izotov et al. (2018) and Rivera-Thorsen et al. (2017). The insets show the two-dimensional Ly α spectra reported with their multiple peaks with indicated the emission '0' close to zero velocity (dotted line; see also Fig. 2 for a detailed view in the case of *Ion2*). The relative escape faction (*fesc*) is also reported in each panel.

C IV $\lambda\lambda$1548, 1550 doublet, He II λ1640, and O III] $\lambda\lambda$1661, 1666 emission lines. The S/N of the He II λ1640 (3.5) is sufficient to appreciate its broadness, plausibly encompassing a velocity interval up to 500 km s^{-1}, marked in Fig. 4 with a segment (see also Appendix B1 for more details). It is worth noting that in other cases the He II λ1640 emission is as narrow as the other high-ionization metal lines (e.g. Vanzella et al. 2016a, 2017c) in which the nebular origin dominates or is better captured and other cases in which both nebular and broader stellar components are measured (Erb et al. 2010; Senchyna et al. 2017, 2019). In the case of *Ion2*, the relative contribution of nebular and stellar components is not measurable. However, the presence of a broad He II λ1640 emission profile suggests a spectrum dominated by a young stellar population containing hot Wolf–Rayet stars with main-sequence lifetimes less than 5 Myr (Chisholm et al. 2019).

(iii) Differently from the previous analysis based on a much shallower Keck/MOSFIRE spectrum in which the optical [O II] $\lambda\lambda$3727, 3729 and H β lines were not detected (de Barros et al. 2016), here we measure a rest-frame equivalent width (EW) of EW(H β) $\simeq$ 100 Å, O32 $= 9.18^{+1.82}_{-1.32}$, and [O III] λ5007/H β $= 8.55^{+1.96}_{-1.41}$ (see Table 1). Such O32 value is in line with the *necessary* condition of having a large O32 index in LyC leakers (Jaskot & Oey 2013; Izotov et al. 2018). It is worth noting that the rest-frame EW of [O III] $\lambda\lambda$4959, 5007 is 1300 Å, not dissimilar from the strong oxygen emitters found at $z > 7$ (e.g. Roberts-Borsani et al. 2016; Castellano et al. 2017). This also suggests a relatively large ionizing photon production efficiency ($\xi_{\rm ion}$), defined as the production rate of H-ionizing photons per unit intrinsic monochromatic UV luminosity ($\xi_{\rm ion} \simeq 25.6$, following Chevallard et al. 2018).[1]

While the Ly α profile further confirms *Ion2* to be a genuine LyC emitter, the detailed geometry of the LyC emission and the origin of the ionizing radiation are still unknown (Vanzella et al. 2016b). Not surprisingly, if the ionized channel and/or the size of the source emitting LyC radiation (namely, the region including O-type stars) is confined within a few tens of pc or less (see Section 3.3), the WFC3/F336W spatial resolution would be insufficient to resolve the source (1 pix $\simeq$ 150 pc). Any further detailed investigation in the rest-frame ultraviolet/optical bands would therefore be postponed to future studies with larger telescopes. Before the advent of E-ELT-like telescopes that will provide a spatial resolution lower than 10 mas (corresponding to $\sim$75 pc at the redshift of *Ion2*), the only way to address individual star-forming complexes of a few tens of pc requires strong gravitational lensing (e.g. Johnson et al. 2017; Rigby et al. 2017; Vanzella et al. 2017c, 2019; Cava et al. 2018). Even more valuable would be the identification of strongly lensed galaxies showing escaping LyC radiation emerging from some of their internal constituents. This happened recently with the discovery of the *Sunbust* arc and is the argument of the next section.

Before discussing it, it is worth stressing that the requirement of having the simultaneous alignment of the ionized channel, the observer, the presence of shot-lived O-type stars, and the transparent IGM along the line of sight implies that the visibility of the LyC radiation from high-redshift sources is affected by severe view angle and line of sight effects (e.g. Wise et al. 2014; Cen & Kimm 2015; Trebitsch et al. 2017), not to mention the insidious foreground contamination mimicking false LyC radiation (e.g. Vanzella et al. 2010, 2012; Siana et al. 2015). Altogether, these effects make the detection of LyC galaxies at high redshift still elusive and suggest that a significant fraction of them might be hidden by the aforementioned effects. Moreover, if we require that the source is also strongly magnified by an intervening gravitational lens, then the event would be extremely rare.[2] The identification of a few LyC galaxies either in non-lensed or lensed fields therefore makes the current detections extremely precious, especially if we focus on the spectral similarities among these uncorrelated objects.

[1]Note that the H α line is not accessible and the H β is detected at low S/N and affected by dust extinction and possibly damped by the LyC leakage.
[2]The lensing cross-section for events with magnification μ exceeding the threshold μ_0 decreases rapidly with the square of the magnification itself: $\sigma_{\rm lens}(> \mu_0) \sim \mu_0^{-2}$.

3 DISCUSSION

To shed more light on the nature of *Ion2*, key information might be extracted by comparing its X-Shooter spectrum to the strongly magnified LyC emitter at $z = 2.37$, dubbed Sunburst arc (Dahle et al. 2016; Rivera-Thorsen et al. 2017, 2019). In this work, we highlight the similarities between such systems arguing that what is observed in Sunburst is compatible with what is currently hidden by the limited spatial resolution.

3.1 The Sunburst arc

Sunburst is an exceptionally bright (R-band magnitude $\sim$18) gravitationally lensed arc in which the galaxy cluster PSZ1-G311 produces a magnification of the order of $\sim$50 or even larger (Dahle et al. 2016). Specifically, four multiple arcs are generated by the galaxy cluster, and in the most magnified ones additional amplification is generated by individual galaxy cluster members. One of the star-forming knots of the arcs has also been detected in the LyC (hereafter dubbed LyC knot) with the unprecedented record of 12 multiple images (Rivera-Thorsen et al. 2019) with a measured magnitude in the interval F814W = [21.5–22] and detected with an S/N > 30 for the most magnified ones.[3]

We present for the first time VLT/MUSE observations targeting the Sunburst and based on the DDT programme 297.A-5012(A) (PI. Aghanim). The data were acquired during 2016 May–August with seeing 0.5–0.8 arcsec for a total integration of 1.2 h (three exposures of 1483 s each). The data reduction has been performed as described in Caminha et al. (2017, 2019), and we refer the reader to those works for details.

A stacked MUSE spectrum obtained from seven multiple images is presented in Fig. 5. In the same figure, some high-quality spectra of local star clusters are shown for comparison (for further details, see the caption of Fig. 5). The ultraviolet emission of the LyC knot resembles those of local super star clusters in which the signatures of massive stars are clearly imprinted in the spectrum, like the prominent P-Cygni profiles of the C IV λλ1548, 1550 doublet and a broad He II λ1640 ascribed to the presence of Wolf–Rayet stars. The similarity with the ultraviolet spectra of a few well-studied local young massive clusters is remarkable, namely R136 (Crowther et al. 2016), II Z40 (Leitherer et al. 2018), and cluster #5 of NG5253 (Smith et al. 2016, see also Calzetti et al. 2015), as well as the analogy with the nearby star-forming regions collected by Senchyna et al. (2017, 2019) and showing high-ionization metal lines and in some cases broad He II λ1640 emission of low-metallicity massive stars. The same spectral features, though at slightly lower S/N ratios, have been identified and accurately modelled by Chisholm et al. (2019), providing a stellar age of 3.0 ± 0.1 Myr and subsolar stellar metallicity $Z = 0.60 \pm 0.05$ $Z_{\odot}$, with an inferred dust extinction $E(B-V) \simeq 0.15$.

While these are very precious quantities and independent from the lensing magnification, it is now natural to try addressing intrinsic quantities such as the stellar mass, the luminosity, and the physical size of such LyC emitter. This will be the argument of the next section.

[3]The magnitudes reported by Rivera-Thorsen et al. (2019) are about half a magnitude fainter than our estimates, while the magnitude contrast among the multiple images is fully consistent with their estimates. As shown in Appendix A, this difference is mainly due to the small aperture they used (0.12 arcsec diameter), motivated by the need to measure the ratio between the ionizing and non-ionizing fluxes of a non-spatially resolved source.

3.2 The Sunburst LyC knot as a possible gravitationally bound system

We express the most relevant physical quantities, namely the effective radius, the stellar mass, and the stellar mass surface density ($\Sigma^{\star}$), as a function of magnification $\mu_{\rm TOT}$, adopting $R_{\rm e} = 2.0$ pix, e.g. 60 mas along the tangential direction as derived by performing `galfit` fitting (see Appendix A and Fig. A2). The stellar mass is estimated assuming an instantaneous burst with the aforementioned age of 3.0 Myr and subsolar metallicity $Z = 0.6$ $Z_{\odot}$, and adopting *Starburst99* models (Leitherer et al. 2014) with a Salpeter initial stellar mass function (IMF; $\alpha = 2.3$), including stars with masses in the range [1–100] $M_{\odot}$. Similarly, we derive the stellar mass using a top-heavy initial stellar mass function with a slope $\alpha = 1.6$, following Jeřábková et al. (2017), with masses in the range [0.1–120] $M_{\odot}$. The two IMFs should embrace two extreme cases with the aim to provide a lower limit and an upper limit to the stellar mass.

As shown in Fig. 6, an effective radius ($R_{\rm e}$) smaller than 20 pc is found if $\mu_{\rm TOT} > 25$, and it decreases below 9 pc if $\mu_{\rm TOT} > 50$. The stellar mass ranges between 10^6 and 10^7 $M_{\odot}$ depending on the IMF and magnification, with a $\Sigma^{\star}$ that enters the regime of the densest objects known (e.g. the globular clusters, e.g. Hopkins et al. 2010) or similar to the values of young massive star clusters (Bastian et al. 2006; Östlin, Cumming & Bergvall 2007; Bastian et al. 2013).

Combining $R_{\rm e}$ with the age of 3.0 Myr, and the stellar mass, we can infer the dynamical age as $\Pi = {\rm Age}/T_{\rm cr}$ [where $T_{\rm cr}$ is the crossing time: $10(R_{\rm e}^3/{\rm GM})^{0.5}$, Gieles & Portegies Zwart 2011]. Interestingly, as highlighted in Fig. 6, the system enters the regime of a gravitationally bound object ($\Pi > 1$) if $\mu_{\rm TOT} > 25(50)$ in the case of Salpeter(top-heavy) IMF. Such magnification values are within the expected magnification regime (e.g. Dahle et al. 2016). In particular, a *minimum* model-independent estimate of the magnification of 20 is derived and discussed in Appendix A, based on empirical geometrical constraints. Therefore, the LyC knot might be the first example of a gravitationally bound star cluster discovered at cosmological distance.

3.3 Is also the LyC-galaxy *Ion2* powered by star clusters?

The discovery of a very likely gravitationally bound star cluster at $z = 2.37$ leaking LyC radiation is intriguing because it would imply that the contribution by such systems to the meta-galactic ionizing background is substantial, if not dominant, depending on the UV luminosity function of such objects.

Observationally, Sunburst-like objects in which the LyC leakage emerges from a single massive star cluster of a few pc cannot be spatially resolved even in moderately lensed fields, e.g. $\mu < 20$. Compact SF-clumps at high redshift, either spatially resolved or not, may be dominated by single young massive star clusters (e.g. Zanella et al. 2015; Johnson et al. 2017; Rigby et al. 2017).

Any seeing-limited spectrum would be the luminosity-weighted average of multiple unresolved star-forming complexes, as for the case of *Ion2* in which structures smaller than 200 pc cannot be resolved. However, the similitude among the spectral properties of *Ion2* and Sunburst is intriguing and might offer new clues, beyond the limitation due to the spatial resolution. The ionized channels traced by the triple-peaked Ly α profiles – especially the narrow peak at systemic velocity – of *Ion2*, *Ion3*, and Sunburst (including the local system of Izotov et al. 2018) might suggest

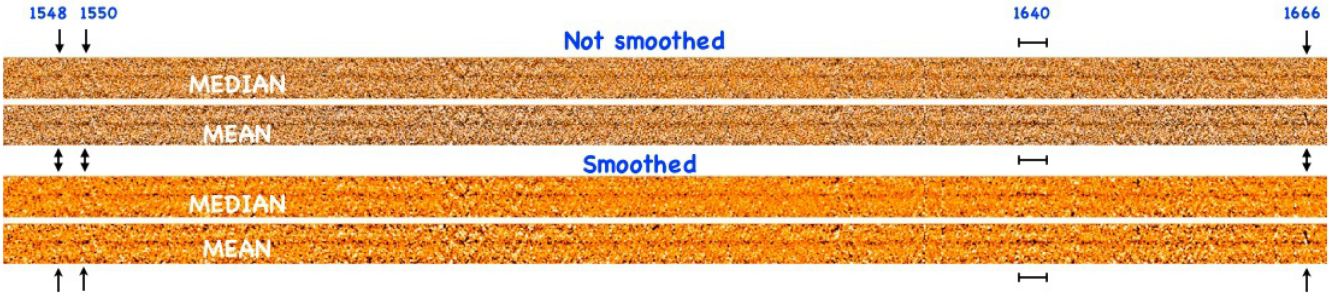

Figure 4. The two-dimensional X-Shooter spectrum of *Ion2* reporting the faint continuum and the C IV λλ1548, 1550, He II λ1640, and O III] λλ1661, 1666 emission lines is shown (indicated with arrows and a segment for the He II λ1640 emission). This figure shows the different broadness of the lines: the width of the segment is ∼500 km s^{-1}, whereas the other C IV λλ1548, 1550 and O III] λλ1661, 1666 lines are much narrower and possibly not resolved (σ_v < 25 km s^{-1}). The top panels show the non-smoothed mean and median spectra. The same is reported in the bottom panels after applying a Gaussian smoothing with $\sigma = 1$ pixel.

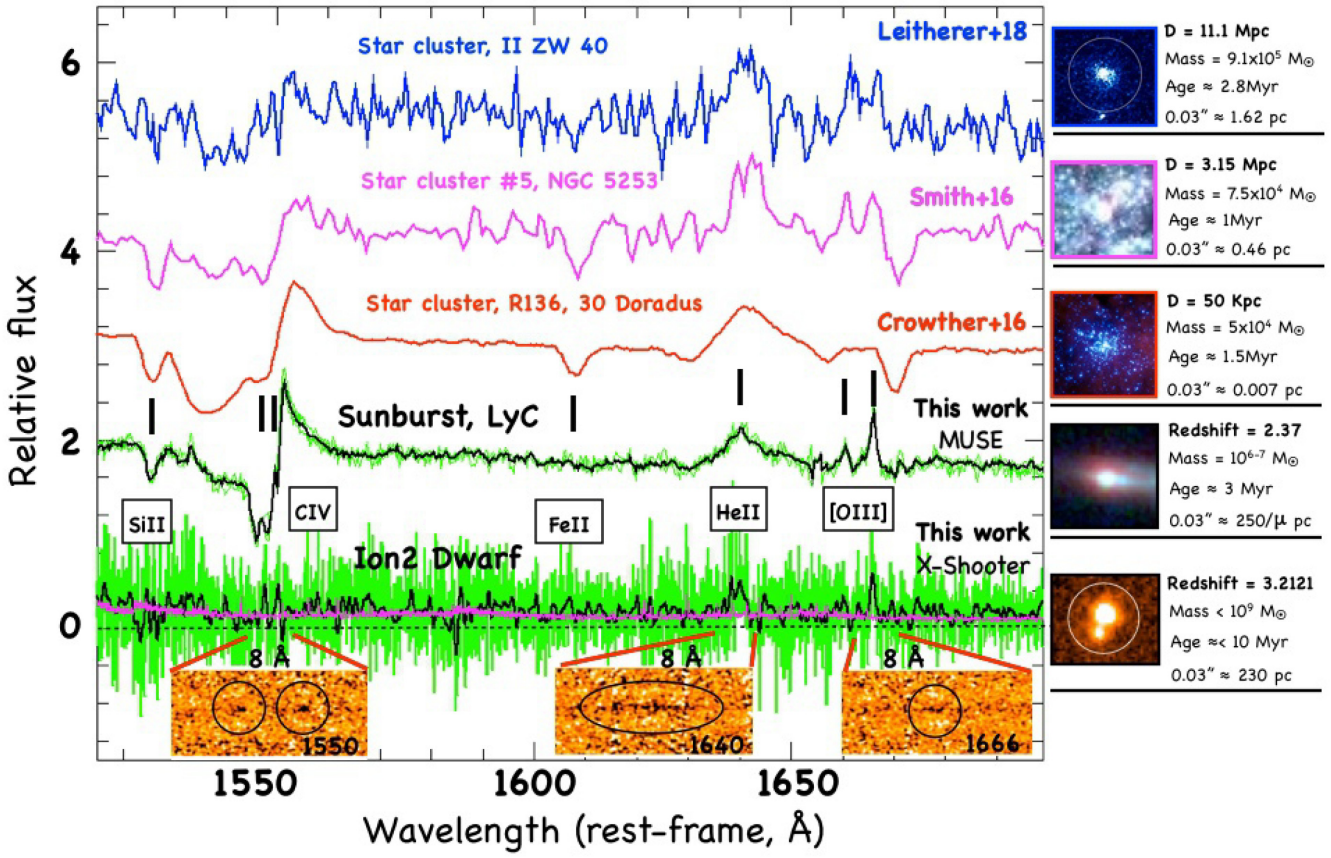

Figure 5. The ultraviolet spectra of local super star clusters (SSCs), the Sunburst, and the *Ion2* are shown. The strongly lensed Sunburst MUSE spectrum (black line as the sum of seven multiple images, plotted with green lines) is remarkably similar to local SSCs. The spectra of *Ion2* at the original spectral resolution (green) and smoothed at the MUSE resolution (black) show nebular metal lines with a broad He II λ1640 emission, as visible from the three insets at the bottom. On the right-hand side, some basic information on each system is reported, including distance (in Mpc), stellar mass (M$_\odot$), age (in Myr), and size (in arcsec and pc). In the case of Sunburst, the size is a function of the magnification μ, estimated to be of the order of 50–100 (Dahle et al. 2016).

a common origin related to the presence of young massive star clusters and/or dense star-forming regions. The *HST* imaging of *Ion2* shows a quite nucleated morphology (the LyC emission is spatially unresolved, Vanzella et al. 2016b), as well as the triple-peaked Ly α object of Izotov et al. (2018) that shows the highest star formation rate surface density (>500 M$_\odot$ yr^{-1} kpc^{-2}) in their sample. Currently, the Sunburst LyC knot seems to be the densest stellar LyC leaker with also emergent Ly α at systemic velocity. In addition, the broad He II λ1640 emission observed in *Ion2* (possibly with FWHM > 400 km s^{-1}, see appendix B) and the well-detected N V λ1240 P-Cygni profile of *Ion3* (Vanzella et al. 2018) suggest a radiation leakage through one or more channels carved by massive stars promoted by their energetic feedback might be in place, as observed in the Sunburst.

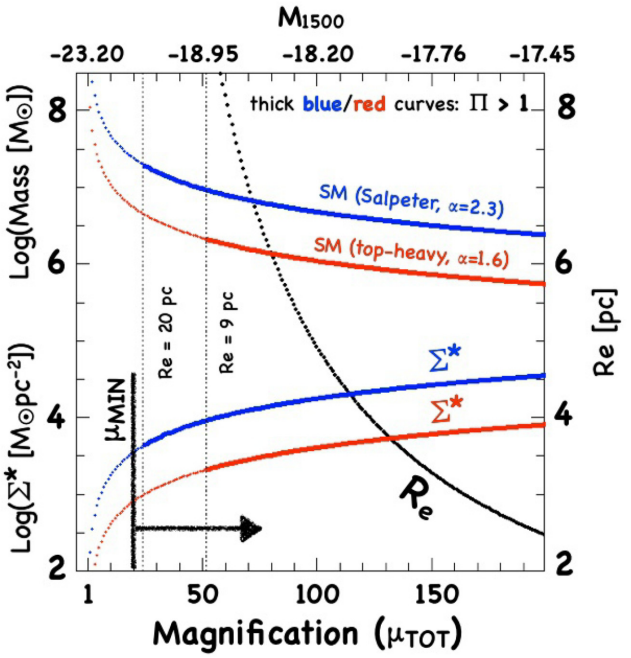

Figure 6. The stellar mass, stellar mass surface density ($\Sigma^{\star}$), and the effective radius (R_e, on the right *Y*-axis) of the Sunburst LyC knot are calculated as a function of the total magnification, μ_{TOT}. The red and blue curves correspond to top-heavy and Salpeter IMF, respectively. The LyC knot becomes compatible with a gravitationally bound star cluster if $\mu_{TOT} > 25(50)$. This regime ($\Pi > 1$) is highlighted with the thick lines, where $\Sigma^{\star}$ approaches the values measured in the densest objects known, like globular clusters and young massive clusters. The thick black horizontal arrow in the bottom marks the minimum magnification, $\mu_{TOT} > 20$, we estimate in Appendix A.

4 CONCLUDING REMARKS

In this paper, we have presented new VLT/X-Shooter observations of the LyC emitting galaxy *Ion2* and VLT/MUSE spectrum of a strongly lensed LyC emitter, dubbed Sunburst. The results can be summarized as follows:

(i) *Ion2*: The spectral resolution and wavelength coverage provided by X-Shooter have improved the previous analysis presented in de Barros et al. (2016), including the detection of new spectral features. First, a multipeaked Ly α profile is evident from the new spectrum, showing a clear emission at the systemic redshift. Secondly, several high-ionization ultraviolet nebular narrow lines (FWHM < 50 km s^{-1}, including C IV $\lambda\lambda$1548, 1550, O III] $\lambda\lambda$1661, 1666, C III] $\lambda\lambda$1907, 1909) have been detected for the first time, some of which with well-separated doublets. Only the He II λ1640 is detected as a broad emission (FWHM > 400 km s^{-1}) and ascribed to the presence of Wolf–Rayet stars. Thirdly, a large value for the O32 index of $9.18^{+1.82}_{-1.32}$ has been derived, together with the large equivalent width of 1300 Å rest frame of [O III] $\lambda\lambda$4959, 5007, as found in other LyC leakers (Jaskot & Oey 2013; Izotov et al. 2018) and typical of systems with a large ionizing photon production efficiency (e.g. Chevallard et al. 2018).

(ii) *Sunburst*: We inferred for the first time the stellar mass (a few 10^6 M$_{\odot}$), luminosity ($M_{UV} > -19$), and size ($R_e < 20$ pc) of the LyC knot of the Sunburst arc, which coupled with the young age of 3 Myr (Chisholm et al. 2019) provides constraints on its dynamical age, suggesting that the LyC knot is a gravitationally bound young massive stellar cluster at cosmological distance, whose ultraviolet spectrum is also fully comparable to those of local young clusters (Fig. 5). In addition, as the Fig. 6 shows, the stellar mass surface density is intriguingly large if the magnification factor exceeds 50, approaching the values observed in the densest objects, such as globular clusters and local young massive clusters (Bastian et al. 2006; Östlin et al. 2007; Hopkins et al. 2010; Bastian et al. 2013). Remarkably, Sunburst might also be considered a forming globular cluster, caught when the Universe was 2.7 Gyr old. This will be investigated in a future work.

The LyC knot of the Sunburst arc might very well represent the Rosetta stone of stellar ionization at high redshift and it is an unprecedented discovery in its own right for two reasons: (1) it is a unique laboratory where the escaping LyC from a high-redshift stellar system can be investigated in detail and (2) without any lensing effect, the LyC knot (the star cluster) would have appeared like a non-spatially resolved LyC emitter lying somewhere within its hosting galaxy, e.g. like *Ion2*.

Interesting enough, the star cluster formation efficiency, namely the star formation occurring in gravitationally bound star clusters, increases with redshift (e.g. Pfeffer et al. 2018), possibly reaching values higher than 30 per cent at $z > 6$. This might suggest that star clusters could have played a significant role during reionization (Ricotti 2002; Ricotti, Parry & Gnedin 2016), especially if the LyC leakage is more efficient for that population. The idea that such young massive star clusters (or a fraction of them) were also globular cluster precursors is currently a matter of investigation (e.g. Calura et al. 2015, 2019; Bouwens et al. 2017; Renzini 2017; Elmegreen 2018; Pfeffer et al. 2018; Kruijssen 2019; Li & Gnedin 2019; Pozzetti, Maraston & Renzini 2019; Reina-Campos et al. 2019; Vanzella et al. 2019).

While the direct detection of LyC radiation at $z > 3$ is challenging and requires that special conditions are realized in the source, with current sensitivity, the effect that the transverse LyC leakage has on the surrounding medium might be easily detectable. Objects like *Ion2/Ion3* or Sunburst having transverse leakage of LyC radiation could induce spatially offset Ly α or Balmer series fluorescence (e.g. Mas-Ribas et al. 2017). Spatially offset Ly α emission/nebulae routinely detected with integral field spectrographs (like MUSE) might represent a viable tool to search for possible local escaping ionizing radiation around star-forming galaxies (e.g. Vanzella et al. 2017a,c; Gallego et al. 2018; Wisotzki et al. 2018).

Finally, the prospects for future investigations of star formation at very small scales – down to single star clusters – at cosmological distance appear very promising. In particular, objects like Sunburst LyC knot stretched by magnification factors larger than 30 will be probed down to FWHM (or pixel-scale) of 6(2) and 3(0.4) pc by VLT/MAVIS and ELT MAORY-MICADO, respectively. These two MCAO-assisted[4] instruments will be also complementary in terms of wavelength coverage, probing the ultraviolet and optical rest-frame wavelengths. Integral field spectroscopy at VLT or ELT will also probe the spatial distribution of nebular high-ionization lines, as a signature of possible stellar mass segregation in star complexes and providing maps at pc scale opening for two-dimensional studies of feedback mechanisms and star formation processes (e.g. James et al. 2016), at cosmological distances.

ACKNOWLEDGEMENTS

We thank the referees for providing detailed comments and suggestions about the reorganization of the manuscript. We thank C.

[4]MCAO = Multi Conjugate Adaptive Optics.

Leitherer, L. Smith, and P. Crowther for providing the ultraviolet spectra of the star clusters shown in Fig. 5. We thank A. Renzini and A. Adamo for stimulating discussions about the possible origin of the LyC knot. EV also thanks J. Chisholm and E. Rivera-Thorsen for stimulating discussions about the Sunburst system. EV thanks T. Jerabkova for fruitful interaction about the IMF used in this work. EV also thanks M. Gronke for useful discussions about the Lyα profile. AM acknowledges funding from the INAF PRIN-SKA 2017 programme 1.05.01.88.04. KC acknowledges funding from the European Research Council through the award of the Consolidator Grant ID 681627-BUILDUP. We also acknowledge funding from the INAF for 'interventi aggiuntivi a sostegno della ricerca di main-stream dell'INAF'.

REFERENCES

Bastian N., Saglia R. P., Goudfrooij P., Kissler-Patig M., Maraston C., Schweizer F., Zoccali M., 2006, A&A, 448, 881
Bastian N., Schweizer F., Goudfrooij P., Larsen S. S., Kissler-Patig M., 2013, MNRAS, 431, 1252
Behrens C., Dijkstra M., Niemeyer J. C., 2014, A&A, 563, A77
Bian F., Fan X., McGreer I., Cai Z., Jiang L., 2017, ApJ, 837, L12
Bik A., Östlin G., Menacho V., Adamo A., Hayes M., Herenz E. C., Melinder J., 2018, A&A, 619, A131
Bouwens R. J. et al., 2017, preprint (arXiv:1711.02090)
Calura F., Few C. G., Romano D., D'Ercole A., 2015, ApJ, 814, L14
Calura F., D'Ercole A., Vesperini E., Vanzella E., Sollima A., 2019, preprint (arXiv:1906.09137)
Calzetti D. et al., 2015, ApJ, 811, 75
Caminha G. B. et al., 2017, A&A, 600, A90
Caminha G. B. et al., 2019, preprint (arXiv:1903.05103)
Castellano M. et al., 2017, ApJ, 839, 73
Cava A., Schaerer D., Richard J., Pérez-González P. G., Dessauges-Zavadsky M., Mayer L., Tamburello V., 2018, Nat. Astron., 2, 76
Cen R., Kimm T., 2015, ApJ, 801, L25
Chevallard J. et al., 2018, MNRAS, 479, 3264
Chisholm J. et al., 2018, A&A, 616, A30
Chisholm J. et al., 2019, preprint (arXiv:1905.04314)
Crowther P. A. et al., 2016, MNRAS, 458, 624
Dahle H. et al., 2016, A&A, 590, L4
Dayal P., Ferrara A. , 2018, Phys. Reports, 780, 1
de Barros S. et al., 2016, A&A, 585, A51
Elmegreen B. G., 2018, ApJ, 869, 119
Erb D. K., Pettini M., Shapley A. E., Steidel C. C., Law D. R., Reddy N. A., 2010, ApJ, 719, 1168
Fletcher T. J., Tang M., Robertson B. E., Nakajima K., Ellis R. S., Stark D. P., Inoue A., 2019, ApJ, 878, 87
Gallego S. G. et al., 2018, MNRAS, 475, 3854
Gazagnes S., Chisholm J., Schaerer D., Verhamme A., Rigby J. R., Bayliss M., 2018, A&A, 616, A29
Gieles M., Portegies Zwart S. F., 2011, MNRAS, 410, L6
Grazian A. et al., 2017, A&A, 602, A18
Gronke M., Bull P., Dijkstra M., 2015, ApJ, 812, 123
Heckman T. M. et al., 2011, ApJ, 730, 5
Herenz E. C., Hayes M., Papaderos P., Cannon J. M., Bik A., Melinder J., Östlin G., 2017, A&A, 606, L11
Hopkins P. F., Murray N., Quataert E., Thompson T. A., 2010, MNRAS, 401, L19
Izotov Y. I., Worseck G., Schaerer D., Guseva N. G., Thuan T. X., Fricke V., Orlitová I., 2018, MNRAS, 478, 4851
James B. L., Auger M., Aloisi A., Calzetti D., Kewley L., 2016, ApJ, 816, 40
Japelj J. et al., 2017, MNRAS, 468, 389
Jaskot A. E., Oey M. S., 2013, ApJ, 766, 91
Jeřábková T., Kroupa P., Dabringhausen J., Hilker M., Bekki K., 2017, A&A, 608, A53
Johnson T. L. et al., 2017, ApJ, 843, L21
Kehrig C., Vílchez J. M., Guerrero M. A., Iglesias-Páramo J., Hunt L. K., Duarte-Puertas S., Ramos-Larios G., 2018, MNRAS, 480, 1081
Kneib J.-P., Natarajan P., 2011, A&AR, 19, 47
Kruijssen J. M. D., 2019, MNRAS, 486, L20
Leitherer C., Byler N., Lee J. C., Levesque E. M., 2018, ApJ, 865, 55
Leitherer C., Ekström S., Meynet G., Schaerer D., Agienko K. B., Levesque E. M., 2014, ApJS, 212, 14
Li H., Gnedin O. Y., 2019, MNRAS, 486, 4030
Marchi F. et al., 2018, A&A, 614, A11
Mas-Ribas L., Hennawi J. F., Dijkstra M., Davies F. B., Stern J., Rix H.-W., 2017, ApJ, 846, 11
Matthee J., Sobral D., Gronke M., Paulino-Afonso A., Stefanon M., Röttgering H., 2018, A&A, 619, A136
McKinney J. H., Jaskot A. E., Oey M. S., Yun M. S., Dowd T., Lowenthal J. D., 2019, ApJ, 874, 52
Micheva G., Oey M. S., Jaskot A. E., James B. L., 2017, ApJ, 845, 165
Micheva G., Herenz E. C., Roth M. M., Östlin G., Girichidis P., 2019, A&A, 623A, 145
Östlin G., Cumming R. J., Bergvall N., 2007, A&A, 461, 471
Pfeffer J., Kruijssen J. M. D., Crain R. A., Bastian N., 2018, MNRAS, 475, 4309
Pozzetti L., Maraston C., Renzini A., 2019, MNRAS, 485, 5861
Reddy N. A., Steidel C. C., Pettini M., Bogosavljević M., 2016, ApJ, 828, 107
Reddy N. A. et al., 2018, ApJ, 869, 92
Reina-Campos M., Kruijssen J. M. D., Pfeffer J. L., Bastian N., Crain R. A., 2019, MNRAS, 486, 5838
Renzini A., 2017, MNRAS, 469, L63
Ricotti M., 2002, MNRAS, 336, L33
Ricotti M., Parry O. H., Gnedin N. Y., 2016, ApJ, 831, 204
Rigby J. R. et al., 2017, ApJ, 843, 79
Rivera-Thorsen T. E. et al., 2017, A&A, 608, L4
Rivera-Thorsen T. E. et al., 2019, preprint (arXiv:1904.08186)
Roberts-Borsani G. W. et al., 2016, ApJ, 823, 143
Schaerer D., Hayes M., Verhamme A., Teyssier R., 2011, A&A, 531, A12
Schaerer D., Izotov Y. I., Verhamme A., Orlitová I., Thuan T. X., Worseck G., Guseva N. G., 2016, A&A, 591, L8
Senchyna P., Stark D. P., Chevallard J., Charlot S., Jones T., Vidal-García A., 2019, MNRAS, 488, 3492
Senchyna P. et al., 2017, MNRAS, 472, 2608
Shapley A. E., Steidel C. C., Strom A. L., Bogosavljević M., Reddy N. A., Siana B., Mostardi R. E., Rudie G. C., 2016, ApJ, 826, L24
Siana B. et al., 2015, ApJ, 804, 17
Smith L. J., Crowther P. A., Calzetti D., Sidoli F., 2016, ApJ, 823, 38
Steidel C. C., Bogosavljević M., Shapley A. E., Reddy N. A., Rudie G. C., Pettini M., Trainor R. F., Strom A. L., 2018, ApJ, 869, 123
Trebitsch M., Blaizot J., Rosdahl J., Devriendt J., Slyz A., 2017, MNRAS, 470, 224
Vanzella E., Siana B., Cristiani S., Nonino M., 2010, MNRAS, 404, 1672
Vanzella E. et al., 2012, ApJ, 751, 70
Vanzella E. et al., 2015, A&A, 576, A116
Vanzella E. et al., 2016a, ApJ, 821, L27
Vanzella E. et al., 2016b, ApJ, 825, 41
Vanzella E. et al., 2017a, MNRAS, 465, 3803
Vanzella E. et al., 2017b, MNRAS, 467, 4304
Vanzella E. et al., 2017c, ApJ, 842, 47
Vanzella E. et al., 2018, MNRAS, 476, L15
Vanzella E. et al., 2019, MNRAS, 483, 3618
Verhamme A., Orlitová I., Schaerer D., Izotov Y., Worseck G., Thuan T. X., Guseva N., 2017, A&A, 597, A13
Wise J. H., Demchenko V. G., Halicek M. T., Norman M. L., Turk M. J., Abel T., Smith B. D., 2014, MNRAS, 442, 2560
Wisotzki L. et al., 2018, Nature, 562, 229
Zanella A. et al., 2015, Nature, 521, 54

APPENDIX A: AN EMPIRICAL MINIMUM MAGNIFICATION FOR THE SUNBURST LYC KNOT

The substructures and star-forming knots present in the Sunburst arcs allow us to set empirical constraints on the minimum (average) magnification among the recognized multiple patterns. Fig. A1 shows the four arcs labelled I, II, III and IV, within which 12 multiple images of the LyC knot (indicated with 'A') have been discovered by Rivera-Thorsen et al. (2019) and are marked with increasing numbers 1–12. In particular, the least magnified arcs provide the less distorted version of the high-z SF complex. Starting from the smallest arc III, the knots A, B, and C are identified in the counter arc IV, with the inverse order (mirroring) of the SF knots as expected in strongly lensed multiple images. In this case, the identification is further facilitated by the fact that the knot A has the distinctive LyC feature and the image C is the most elongated among the three objects. Such features must follow the aforementioned flipped behaviour, accordingly to the parity of the images introduced by the strong lensing (Kneib & Natarajan 2011). Other two triplets A, B, and C appear in the arc II where the mirrored groups are circled with green dotted ellipses. The triplet separated by 3.72 arcsec is 10 times more elongated than the triplet in the arc III, which means that the average tangential magnification for the widest arc is larger than 10, being the magnification of arc III larger than 1.

The situation of arc I is different because not all images (A, B, and C) are present, i.e. only a part of the source is multiply lensed in this merging arc. However, six multiple images of knot A (the LyC emitter) are clearly identified (images 1–6 of Fig. A1). The proximity of some of the images to the critical lines, like images 2 and 3, suggests that the magnification is large (see e.g. fig. 4 of Rivera-Thorsen et al. 2019). In particular, the measured flux ratio between images 2 (or equivalently 3) and 8 is $\simeq$2 (Rivera-Thorsen et al. 2019), suggesting images 2 and 3 have a minimum magnification of $\sim$20 (2 $\times$ 10). The same happens for the brightest image 10, which is 2.2 times brighter than image 8. Until this point, we did not invoke any lens model. The true magnification is higher since we are assuming that arc IV is not magnified ($\mu = 1$). However, arc IV is subjected by strong lensing as well (being one of the multiple images of the system) and its magnification is certainly higher than 1. For example, assuming a magnification 2 for arc IV, following the aforementioned considerations the magnification for images 2 and 3 jumps to values of 40. This provides an average magnification, and as discussed above the proximity to the critical

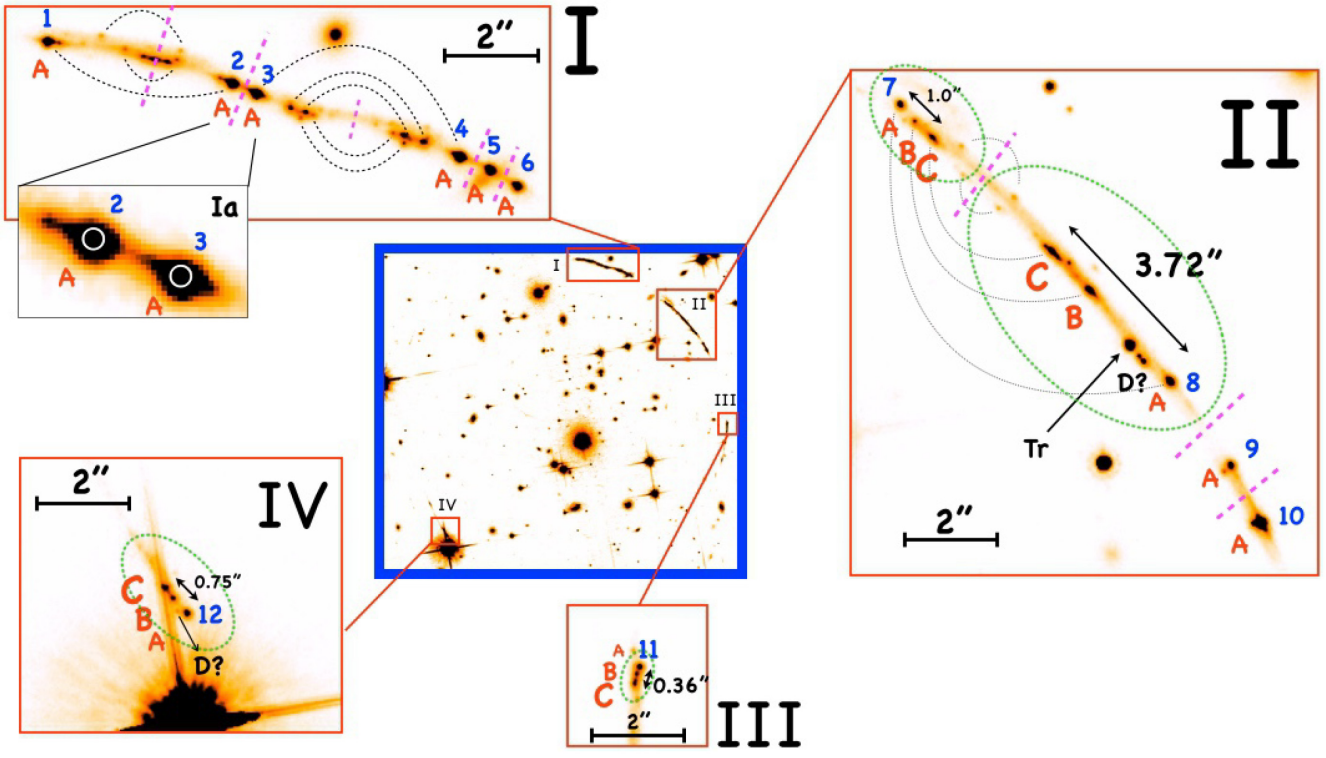

Figure A1. A complete overview of the four arcs is shown in the central panel with the zoomed regions shown clockwise (panels I, II, III, and IV). The tangential stretch is clearly visible after the identification of the three knots A, B, and C. The knot A is the LyC knot discussed in this work and its distinctive signature allows a secure identification (Rivera-Thorsen et al. 2019). In particular, the ratio among the angular separations between A-C for the less magnified system (III) and the most stretched one (II) implies an average tangential magnification larger than 10 for system II (i.e. knowing the arc III has $\mu > 1$). The relative flux ratio among the LyC knots 2 (or 3) and image 8 of $\simeq$2 further implies that the magnification for images 2 (or 3) is higher than 20. The magenta dotted lines mark approximately the locations where the critical lines cross the arcs (for the arc I, see also Rivera-Thorsen et al. 2019). The dotted green ellipses highlight the multiple structures containing the knots A, B, and C and other small features. Some of the mirrored multiple images within the arcs (accordingly with the parity of the images generated by strong lensing, Kneib & Natarajan 2011) and tiny SF knots are connected with the dotted black lines. Other substructures are marked with 'D' and are visible only in the most magnified regions (or represent foreground sources). Finally, another bright object not present in any of the other arcs is marked as 'Tr' in panel II and represents a possible transient (Vanzella et al. in preparation). The inset Ia shows a zoom of the images 2 and 3 and highlights the circular apertures used in Rivera-Thorsen et al. (2019) to derive the F814W magnitudes reported in their table 1. While such a small aperture is appropriate for their goals (measure of the ionizing-to-non-ionizing flux ratio for a point-like object), our magnitudes derived with `galfit` fitting in the F814W band account for the total flux and spatially resolved morphology, making our estimates closer to the total magnitude.

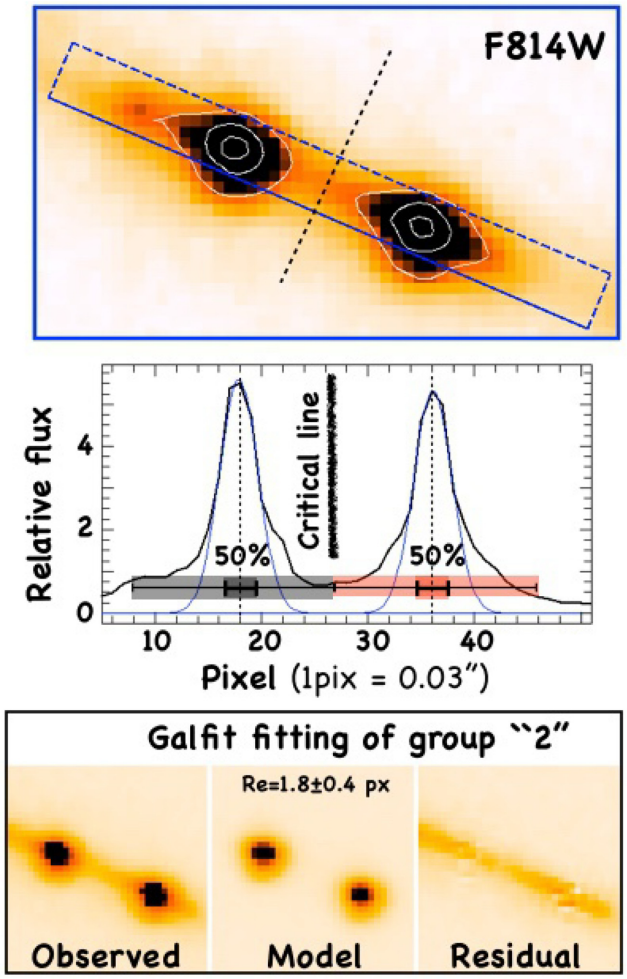

Figure A2. The top panel shows the F814W zoomed image of the multiple images '2' and '3' with the rectangular aperture (1.6 arcsec × 0.13 arcsec) used to calculate the profiles reported in the middle panel, in which the 50 per cent area along the tangential direction is highlighted (shaded regions), and the FWHM (0.13 arcsec) of the F814W band is superimposed with a blue line. The expected crude position of the critical line is also indicated. The symmetry of the profiles (also outlined with the white contours in the F814W images, in the top panel) despite the vicinity of the knots to the critical line (0.26 arcsec) suggests that the objects are quite compact. In the bottom, the `galfit` solution in the same band is also shown, with a Sersic index 4.0 and effective radius $\lesssim$2 pixel (see the text for details).

lines suggests that the lensing amplification at the position of, e.g. images 2 and 3 could be much higher, even above 50 as discussed by Dahle et al. (2016). A careful modelling of the lens, including the aforementioned empirical constraints, will shed more light on this.

However, the minimum magnification of 20 derived above is already relevant in our study, implying an effective radius smaller than 20 pc and a stellar mass in the range (5×10^6)–(2.5×10^7) $M_\odot$, depending on the IMF (see Fig. 6), with the system entering the range of massive, gravitationally bound, star clusters in the case of Salpeter IMF.

It is worth noting the presence of a bright and point-like object with F814W = 22.02 and at the same redshift of the Sunburst (marked with 'Tr' and an arrow in Fig. A1). Such an object is presumably a transient for two reasons: (1) it is not identified in any of the other arcs and (2) it shows unique spectral properties in the MUSE spectrum not observed in any of the other knots populating the rest of the arcs (the ongoing X-Shooter programme[5] will investigate 'Tr' and the results presented elsewhere). The characterization of such a transient (like the absolute magnitude) will provide a unique constraint for the lens model.

Fig. A2 shows the two multiple images '2' and '3', each one located 0.26 arcsec away from the critical line, which necessarily falls between them. The giant arc-like shape also implies that the magnification is mainly tangential, such that the total magnification is close to the tangential one, $\mu_{\rm TOT} \simeq \mu_{\rm tan}$ (see the discussion in Vanzella et al. 2017b). Despite the fact that the knots lie in a region with a potentially steep tangential magnification gradient, the light profiles along the same direction are symmetric (see Fig. A2, middle panel), strongly supporting the fact that the object is intrinsically compact (see also the discussion by Vanzella et al. 2016a on another similar case). As shown in the middle panel of the same figure, the LyC knot is marginally resolved in the *HST*/F814W image, close to the resolution in that band, in which the PSF FWHM is $\simeq$0.13 arcsec (though it is not a point-like source). Indeed, specific `galfit`-based deconvolution analysis (as similarly performed in Vanzella et al. 2016a, 2017b) produces effective radii ($R_{\rm e}$) of the order of 1.0–2.0 pixel, for a Sersic index in the range $n = 0.5$–5. It is worth noting, however, that a large n and $R_{\rm e}$ would produce non-symmetric tangential profiles, as mentioned above. This will be fully investigated with dedicated simulations of all the knots and the emerging light profiles by placing objects with known structural parameters in the source plane close to the caustics (see appendix A of Vanzella et al. 2017b), once the lens model will be developed.

APPENDIX B: MEASURING THE SIGNIFICANCE OF THE EMISSION LINES DETECTED IN THE X-SHOOTER SPECTRUM

The statistical significance of the emission lines reported in Table 1 has been calculated performing spectral scans over the reduced spectra in the UVB, VIS, and NIR arms. In particular, we describe here the case of the VIS arm, in which we explore the presence and broadness of the He II λ1640 line.

A spectral scan over the two-dimensional reduced spectrum is performed by using a window with spatial scale *ds* and velocity *dv*. *ds* has been fixed to 0.8 arcsec, slightly larger than the mean seeing during the observations (the spatial scale in the VIS arm is 0.16 arcsec/pix). Three velocity widths have been used, $dv = 200$, 450, and 900 km s^{-1}. Small(large) *dv* captures small(large) spectral features. The scan has been performed pixel by pixel in the wavelength direction (0.2 Å/pix), while the spatial direction windows do not overlap with each other (they are independent). Moreover, we distinguished between the position of the target (which lies at a fixed position) and the rest of the slit. After excluding the target and the edges of the slit, we end up with 10 independent windows corresponding to each wavelength position. Fig. B1 shows the results of this exercise. The black line in each panel shows the scan performed at the position of the target. The scan with small *dv* recovers the narrow features and doublets discussed in the text, like the C IV λλ1548, 1550, O III] λλ1661, 1666, He II λ1640, and the C III] λλ1907, 1909 lines. The results of the same scan avoiding the target are shown with the blue dots, which are more distributed around the zero value and follow the spectral pattern of the sky

[5]VLT/X-Shooter, P103.A-0688(A-C), PI Vanzella.

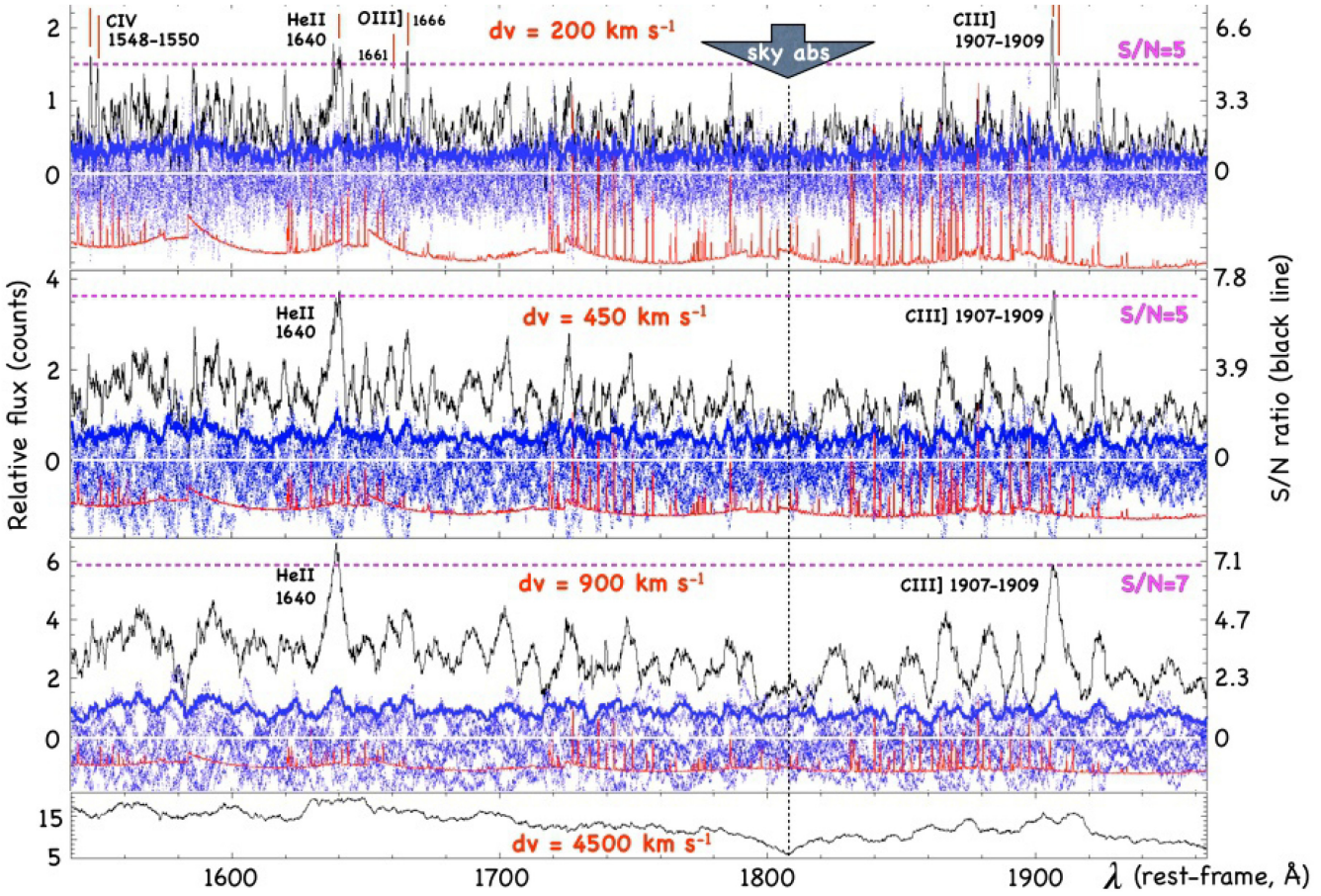

Figure B1. The spectral scan performed in the VIS arm with the aim to quantify the statistical significance of the spectral features of *Ion2* reported in Table 1. As discussed in the text, the scan is performed by using four windows, all of them having the same spatial scale (of 0.8 arcsec) and different velocity widths $dv = 200$, 450, 900, and 4500 km s^{-1}. The black lines show the scan calculated over the target trace. The small/large spectral features are detected with small/large dv, e.g. the narrow doublets and the He II λ1640 emission, respectively. The same scan performed in the region of the spectrum avoiding the position of the target provides an estimate of the error fluctuation in the chosen window (cloud of small blue dots), from which the standard deviation is also extracted and indicated with a thick, nearly flat, blue line. Therefore, the black and thick blue lines represent the signal and the error, respectively. The *Y*-axis on the right indicates the S/N ratio, with the values at S/N = 5 and 7 marked with magenta dashed lines. The position of the sky emission lines and the shape due to the various orders within the VIS arm are shown in red, suitably rescaled for the figure purposes. The 7600 Å sky absorption band (corresponding to rest-frame 1800–1820 Å) is also indicated with a large arrow and is consistent with the dip visible in the continuum of the target in that position. In the bottom panel, $dv = 4500$ km s^{-1}, such a continuum dip is clearly recovered.

emission (shown with the red line and rescaled as a guidance). The thick blue line represents the standard deviation of the cloud of blue points calculated over the 10 windows available at each wavelength position. The black and thick blue lines are the signal and the error, respectively. The S/N ratios reported in Table 1 are inferred from this analysis.

The same spectral scan has been computed by enlarging dv. Fig. B1 clearly shows that as dv increases the tiny spectral features disappear, hidden by the continuum fluctuation. The continuum shows a small (but wide) dip at $\lambda \sim 1810$ Å, which corresponds to 7620 Å at the observed frame, due to the well-known sky absorption band (7600–7640 Å). Two main spectral features associated with *Ion2* stand out from the continuum: the C III] λλ1907, 1909 doublet that is detected as a single entity and the broad emission identified at the position of He II λ1640, with an S/N $\simeq$ 4.

This paper has been typeset from a TEX/LATEX file prepared by the author.